AIP Advances

A thermally robust and thickness independent ferroelectric phase in laminated hafnium zirconium oxide

Cite as: AIP Advances 6, 095123 (2016); https://doi.org/10.1063/1.4964300
Submitted: 24 June 2016 • Accepted: 22 September 2016 • Published Online: 29 September 2016

S. Riedel, P. Polakowski and J. Müller

ARTICLES YOU MAY BE INTERESTED IN

The origin of ferroelectricity in $Hf_{1-x}Zr_xO_2$: A computational investigation and a surface energy model
Journal of Applied Physics 117, 134109 (2015); https://doi.org/10.1063/1.4916707

Grain size engineering for ferroelectric $Hf_{0.5}Zr_{0.5}O_2$ films by an insertion of Al_2O_3 interlayer
Applied Physics Letters 105, 192903 (2014); https://doi.org/10.1063/1.4902072

Stabilizing the ferroelectric phase in doped hafnium oxide
Journal of Applied Physics 118, 072006 (2015); https://doi.org/10.1063/1.4927805

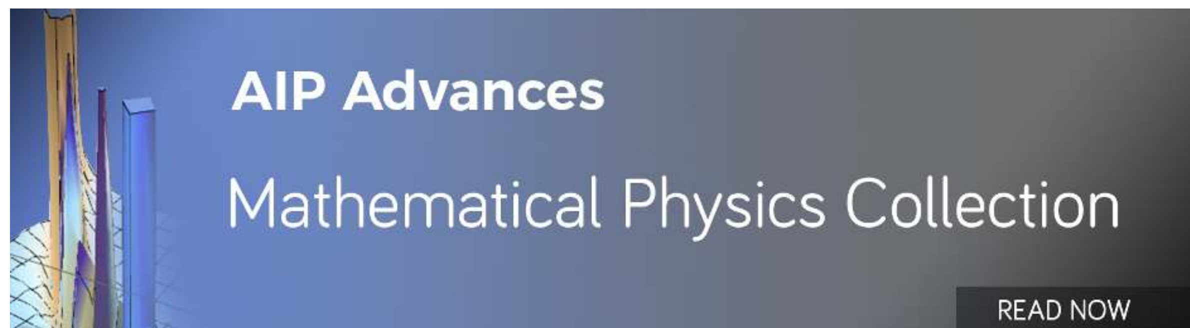

© 2016 Author(s).

AIP ADVANCES **6**, 095123 (2016)

A thermally robust and thickness independent ferroelectric phase in laminated hafnium zirconium oxide

S. Riedel,[a] P. Polakowski, and J. Müller
Fraunhofer IPMS, Königsbrücker Str. 178, 01099 Dresden, Germany

(Received 24 June 2016; accepted 22 September 2016; published online 29 September 2016)

Ferroelectric properties in hafnium oxide based thin films have recovered the scaling potential for ferroelectric memories due to their ultra-thin-film- and CMOS-compatibility. However, the variety of physical phenomena connected to ferroelectricity allows a wider range of applications for these materials than ferroelectric memory. Especially mixed $Hf_xZr_{1-x}O_2$ thin films exhibit a broad compositional range of ferroelectric phase stability and provide the possibility to tailor material properties for multiple applications. Here it is shown that the limited thermal stability and thick-film capability of $Hf_xZr_{1-x}O_2$ can be overcome by a laminated approach using alumina interlayers. © *2016 Author(s). All article content, except where otherwise noted, is licensed under a Creative Commons Attribution (CC BY) license (http://creativecommons.org/licenses/by/4.0/).* [http://dx.doi.org/10.1063/1.4964300]

I. INTRODUCTION

Ferroelectrics are characterized by the existence of spontaneous polarization which is switchable in an external electric field. In order to enable a switching behavior the coercive field strength of the material has to be below the dielectric breakdown field. The ability to program two discrete conditions into these materials renders them promising candidates for semiconductor memories.

Over the last decades this single application has clearly become the major driving force for making ferroelectrics durable, scalable and available to CMOS technology. However, the much broader application space ferroelectrics are best known for is provided by their subgroup relationship to pyroelectrics, piezoelectrics and ultimately dielectrics. Here, although mostly restricted to discrete components, the usage of ferroelectric or antiferroelectric thin films spans from ultrasonic transducers and micro actuators to pyroelectric infrared sensors and high energy storage capacitors.[1] However, the progressive miniaturization in those fields as well as the increasing demand for more and more functionality per chip yields new potential for ferroelectrics which can be integrated into CMOS manufacturing. Especially new tasks such as sensing and energy harvesting clearly reach beyond the pioneering memory applications.

With ferroelectric hafnium oxide (FE-HfO_2) a CMOS-compatible, scalable, 3D-capable and lead-free material emerges that appears ideally suited for this new application space.[2] Primarily motivated by memory applications, thickness scaling to the single digit nanometer range,[3] 3D-capacitor integration,[4] as well as ferroelectric field effect transistor implementation at the 28 nm node[5] has already been demonstrated. First results on non-memory applications of FE-HfO_2 such as negative capacitance FETs[6] or high energy storage capacitors using antiferroelectric hafnium oxide (AFE-HfO_2)[7] have already been reported. However, emerging applications such as piezoelectric or pyroelectric energy harvesters, pyroelectric infrared sensors or the feasibility of a FE-HfO_2 based ferroelectric tunnel junction (FTJ) have yet to be demonstrated.

Compared to the doped FE-HfO_2 systems,[8] which react sensitively to small stoichiometry variations, ferroelectricity in the $Hf_xZr_{1-x}O_2$ solid solution is observed over a broad compositional range,[9] providing a clear advantage in terms of process stability and variability. However, due to the lower

[a]Electronic mail: stefan.riedel@ipms.fraunhofer.de

 © Author(s) 2016

crystallization temperature of ferroelectric $Hf_xZr_{1-x}O_2$ films compared to Si doped or trivalently doped layers premature crystallization during deposition may occur.[10] Furthermore extensive grain growth and grain boundary extension takes place during thermal treatments and high temperature processing steps necessary in CMOS device fabrication. This leads to a degradation of reliability properties and ferroelectric characteristics and limits the applicability of $Hf_xZr_{1-x}O_2$ based materials for FRAM and FeFET devices.[11] A quite similar reliability problem was encountered when ZrO_2 was first suggested as a node dielectric for advanced DRAM manufacturing. To circumvent these issues with pure ZrO_2, Al_2O_3 separated laminates were introduced that came to be known as ZAZ.[12]

In order to address the limitations of the $Hf_xZr_{1-x}O_2$ system in a similar manner we followed up on the approach suggested by H.J. Kim et al.[13] and investigated films laminated with thin alumina layers. The scope of this paper is to explore the limitations of this approach in terms of endurance, thermal stability as well as thick-film- and 3D-capability. Especially in the case of beyond memory applications these are important attributes determining the competitiveness of this material system. We anticipate that due to the large consumption of expensive chip area in system on chip piezoelectric or pyroelectric devices, 3D-capability, which has not yet been demonstrated for $Hf_xZr_{1-x}O_2$ films, will play an important role for future ferroelectric materials. Additionally the output power for piezoelectric harvesting applications increases with the effective volume of the harvesting material.[14] Therefore layer thicknesses in the range of a couple of 100nm to a few µm are usually applied in thin film piezoelectric harvesters. Hence, to enable HfO_2 based systems for this application space their ferroelectric properties need to be independent of thicknesses scaling.

It is worth noting that this thickness independent scaling as already been achieved in films deposited by chemical solution deposition (CSD) in the pioneering work by Starschich et al.[15] However, the multiple heating steps necessary to build up a nano-crystalline thick film, which is a prerequisite to maintain the ferroelectric properties at increased film thickness, raises concerns regarding the manufacturability and 3D-capability of a CSD based process. In this case chemical vapor deposition based methods like ALD, which is established in semiconductor manufacturing, appears highly favorable.

II. EXPERIMENTAL METHODS

The $Hf_xZr_{1-x}O_2$ mixed films (HZO) were deposited by atomic layer deposition (ALD) using a Jusung Eureka 3000 single wafer warm wall reaction chamber. Tetrakis(ethylmethylamino)hafnium (TEMAHf) and Tetrakis(ethylmethylamino)zirconium (TEMAZr) were used as precursors to deposit the HZO films, while ozone was used as co-reactant. The HZO films were deposited by alternating TEMAHf and TEMAZr based processes with a cycle ratio of 1:1 or 2:3 in order to obtain intermixed films. Layers of different thickness were deposited by repeating this supercycle several times. The deposition temperature was 250°C. The saturated growth rate of pure HfO_2 and pure ZrO_2 were both 1Å per cycle leading to a growth per supercycle of 2Å (cycle ratio 1:1) and 5 Å (cycle ratio 2:3), respectively. Layers with an approximate thickness auf 15, 30 and 50nm were deposited in order to investigate the thickness scaling of the ferroelectric properties with a cycle ratio of 1:1. Laminated films were deposited by intercepting the HZO deposition with thin Alumina films. Al_2O_3 was deposited using Trimethylaluminium (TMA), which was supplied by bubbling at room temperature, and ozone. The growth rate of Al_2O_3 was 0.9Å per cycle. 5 and 10 cycles of Al_2O_3 where used as interlayer after each 5 or 10nm of ZrO_2 in order to clarify the influence of lamination on the material system. Titanium nitride was used as top and bottom electrode to form metal ferroelectric metal (MFM) capacitors. The bottom electrodes were deposited by thermal ALD using $TiCl_4$ and NH_3 at 450°C using an ASM A412 batch furnace. The top electrode for planar 2D samples was deposited by sputtering TiN thin films to minimize the thermal stress for the ferroelectric. The samples were subjected to a 650°C/20s rapid thermal anneal in nitrogen ambient in order to form the ferroelectric orthorhombic phase. Selected samples were also annealed at 1050°C/20s in order to prove the increased thermal stability of laminated samples. Samples for electrical characterization were prepared by e-beam evaporating metal dots (5nm Ti glue layer/20nm Pt electrode) on top of the TiN top electrode via a shadow mask. The TiN top electrode was etched using these metal dots as masking layer by an SC1 (NH_4OH:H_2O_2:H_2O 1:2:40) wet etchant at 50°C. Three-dimensional MFM samples

were prepared using a process flow described in detail elsewhere.[4] This process flow uses TiN top electrodes deposited by pulsed CVD at 400°C. The 3D samples were also annealed at 650°C for 20s to guarantee the formation of a crystalline phase.

The composition of the HZO films was determined by x-ray photoelectron spectroscopy on a ReVera Veraflex tool using Al-Kα excitation and analyzer pass energy of 141.2 eV. The collection angle of the spectrometer is 0° with respect to the sample normal. X-ray reflectograms and grazing incidence diffractograms were collected on a Bruker D8 Discover tool equipped with a Cu- Kα Source and a Göbel mirror to create a parallel beam. Scanning transmission electron microscopy (FEI TECNAI F20XT 200 kV acceleration voltage with high angle angular dark field (HAADF-STEM) detector) was used to retrieve structural characteristics, as well as compositional profiles from cross sections. The electrical characterization was performed using a semiautomatic prober (SUSS PA-300) equipped with an aixACCt Systems TF Analyzer 3000 for P-V measurements and an Agilent 4155C Parameter Analyzer for I-V characterization. All samples were cycled for 10^4 cycles before measuring the polarization hysteresis to minimize wake-up effects. The hysteresis was determined using triangular voltage waveforms with a frequency of 10 kHz.

III. RESULTS AND DISCUSSION

In order to investigate the structure of the laminated films XR reflectograms and TEM cross sections were taken. The laminated structure of these films is preserved upon annealing to 650°C as shown by the XR reflectograms which exhibit pronounced superlattice peaks (FIG. 1a).

The laminated structure of the layers is also shown by STEM Micrographs (FIG. 2). Due to the Z-contrast of HAADF-STEM images the low Z alumina layers can be clearly distinguished from the high Z HZO layers for the laminated films (FIG. 2a). Additionally an EDX linescan shows a distinct increase of the intensity of Al-Kα line at the position of the interlayer and a drop in the intensity of the Hf and the Zr lines, which is not detectable at unlaminated samples (FIG. 2c). The apparent increase of the Hf-M (1644eV) intensity at the substrate is caused by the Si- Kα line (1740eV) which overlaps with the Hf-M signal due to the limited resolution of the used EDX detector. Another important difference of laminated to unlaminated films is the significantly increased roughness of unlaminated films caused by the crystallization of the films during deposition. As illustrated by (FIG. 3) a partial crystallization into the monoclinic phase takes place if the film thickness exceeds 30nm.

The polarization-voltage (P-V) results for laminated films of thickness between 5 nm (no Al_2O_3 interlayer) – 50nm (9 Al_2O_3 interlayers) are depicted in FIG. 4. In agreement with[13] it is clearly observed that the ferroelectric properties can be preserved despite the insertion of Al_2O_3 layers. The remanent polarization of all films is around 20μC/cm^2.

A more pronounced benefit of the laminated films appears when comparing the remanent polarization of laminated films with unlaminated $Hf_xZr_{1-x}O_2$ as shown in FIG. 5. Although unlaminated films with a thickness of 15nm show the highest P_r (28μC/cm^2) the remanent polarization drastically drops, with increasing thickness (FIG. 5) to 8μC/cm^2 at a thickness of 50nm. This drop in the

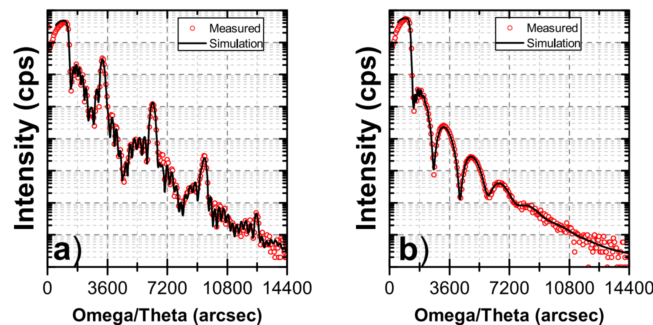

FIG. 1. X-Ray reflectograms taken after 650°C/20s/N_2 anneals of a) a 50nm laminated film on a 10nm TiN electrode. The high intensity peaks are due to the superlattice structure of the film, b) a 50nm unlaminated film on a 10nm TiN electrode. The high frequency oscillation caused by the thick HZO film is strongly damped due to the film roughness.

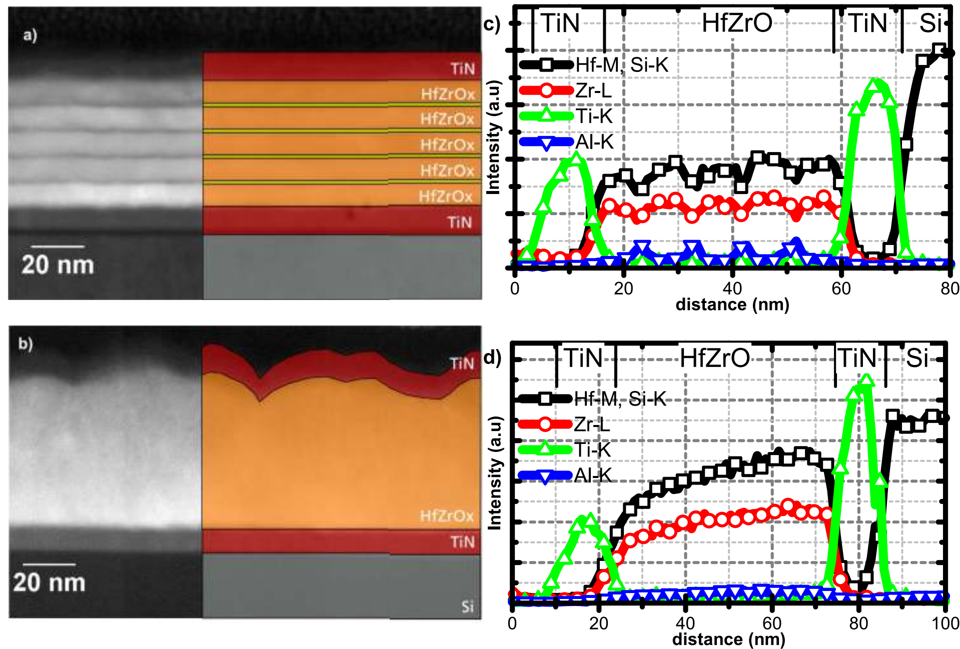

FIG. 2. HAADF-STEM Micrographs (a,b) and EDX linescans (c,d) after 650°C/20s/N_2 anneal of 50nm laminated films (a,c) and 50nm unlaminated films (b,d).

remanent polarization is attributed to an increasing monoclinic phase fraction as proven by grazing incidence x-ray diffractograms (GI-XRD) taken after the crystallization annealing (FIG. 6). Another drawback of unlaminated films is that at high thickness the layers crystallize during deposition as shown by GI-XR diffractograms collected after deposition. Crystallization during film growth leads to

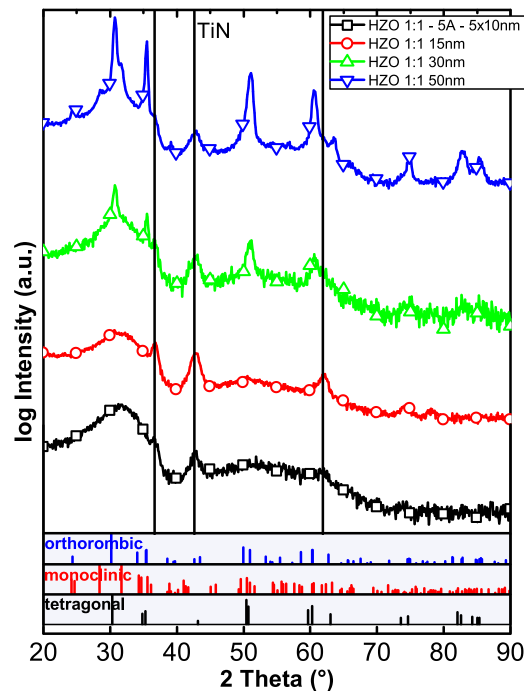

FIG. 3. Grazing incidence x-ray diffractograms (ω =0.5°) taken after deposition. Thin films and laminated films are x-ray amorphous. Unlaminated layers which are thicker than 30nm partially crystalize in the monoclinic phase.

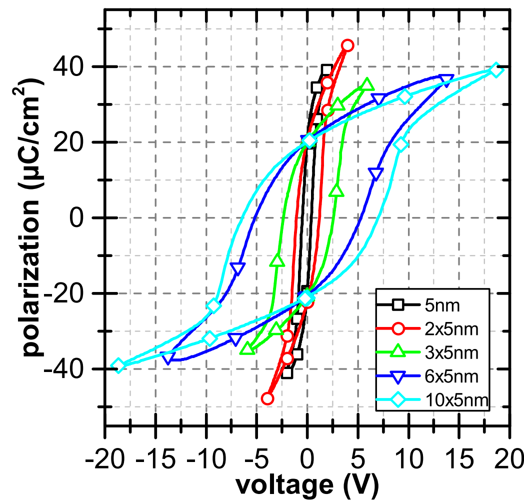

FIG. 4. PV curves of laminated HZO films consisting of an increasing number of HZO single layers after 10^4 cycles. The remanent polarization does not change with increasing overall layer thickness.

the formation of crystalline facets causing an increased layer roughness as shown by XRR (FIG. 1b), which is detrimental to the leakage current and reliability properties of the ferroelectric and dielectrics in general 15, 16.

Furthermore laminated films enable thickness scaling without significant P_r loss. The remanent polarization of the laminated films consisting of stacked 10nm layers is in the same range as the P_r of a single 10nm film (~25-30µC/cm^2, FIG. 5). The same applies for 5nm laminated films with 5cycle Al_2O_3 interlayers (20µC/cm^2). However 5nm films laminated with 10 cycles of Al_2O_3 (FIG. 5) show a distinct P_r-loss. This is attributed to the fact that, with increasing Al_2O_3 thickness and increasing number of interlayers the coercive voltage of the complete stack increases. The PV measurement system used in this study is limited to voltages of +-25V which is insufficient to switch all domains of the films yielding an apparent reduced P_r for the 50nm film. Since the switching voltage is an important parameter for applying these films in actual devices this illustrates that although laminating

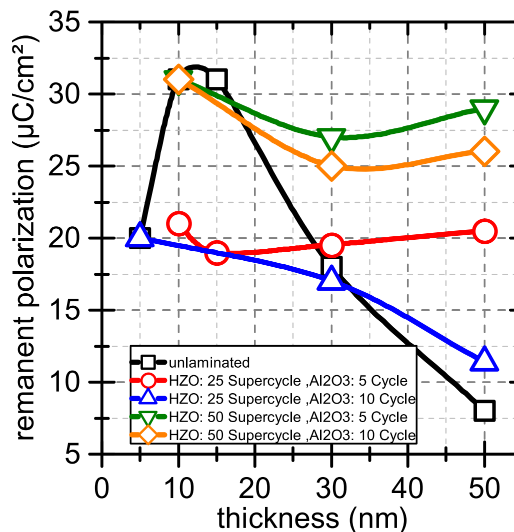

FIG. 5. Remanent polarization in dependence of the laminated structure of the film. The remanent polarization of the single layer is preserved with increasing number of individual HZO films. The polarization of unlaminated films decreases with increasing film thickness.

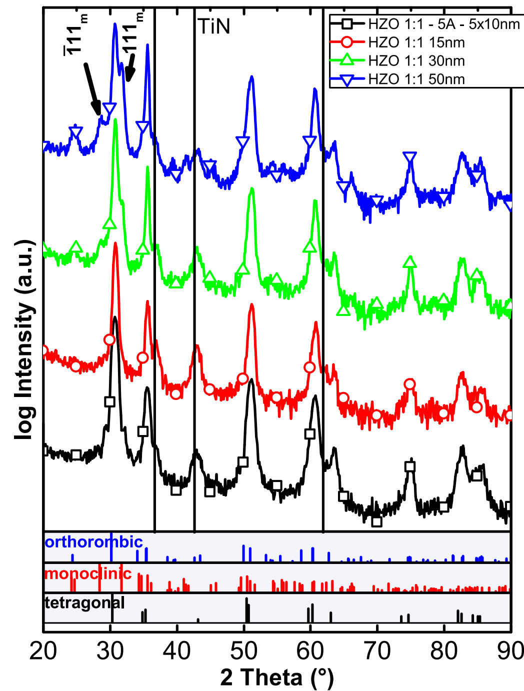

FIG. 6. Grazing incidence x-ray diffractograms (ω =0.5°) taken after annealing (650°C/N_2/20s). The diffraction peaks attributed to the HZO films, which were amorphous after deposition coincide with the orthorhombic phase. The monoclinic phase fraction of thick films is preserved upon annealing.

improves the stability of the ferroelectric behavior the individual thicknesses of the ferroelectric and the interlayer need to be carefully chosen.

Another advantage of laminated films is that the static leakage current is significantly reduced as illustrated in FIG. 7. Especially the leakage current at the coercive field, which is in the range of ∼2MV/cm, depending on the material system, is reduced by more than one order of magnitude. The introduction of thin alumina interlayers prevents the formation of grain boundaries, which run through the complete thin film from the bottom to the top electrode and therefore interrupts a typical

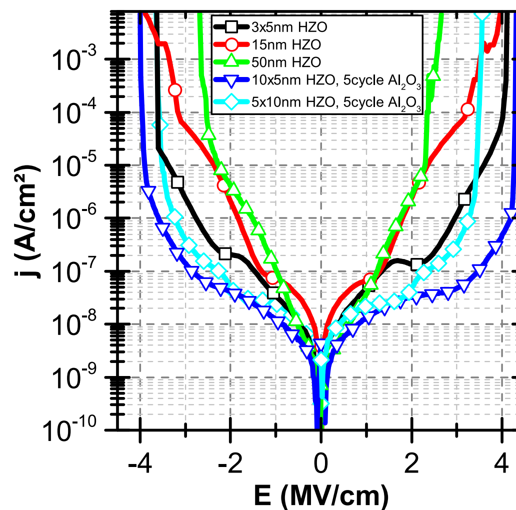

FIG. 7. Leakage current density of laminated and unlaminated films. The leakage current of laminated films is significantly reduced.

leakage current path in crystalline dielectrics.[16] Additionally the breakdown field of the laminated films is increased, which further improves the reliability of the layers.

This reliability improvement becomes obvious, when evaluating the switching endurance of the layers (FIG. 8). A 50nm film laminated with 5 cycles of Al_2O_3 can be cycled 10^7 times before a hard breakdown occurs, whereas unlaminated films experience hard break down after $4*10^5$ cycles. Films, which were deposited using 10 cycles of intermitting alumina, do not show any breakdown up to the maximum investigated cycle number of 10^8.

However, it has to be noted that the laminated films show a distinct fatigue behavior. It is assumed that the Al_2O_3 interlayers create additional charge trapping sites, which are filled during switching. Furthermore, a potential well is created between two individual Al_2O_3 layers due to the higher band gap of Al_2O_3 (8.8eV[17]) compared to $Hf_xZr_{1-x}O_2$ (5.8eV[17]). This potential well hinders the detrapping of charges trapped in the $Hf_xZr_{1-x}O_2$ layer similar to SONOS charge trap devices. The electric fields induced by trapped charge are opposed to the fields created by the ferroelectric dipoles leading to a diminishing remanent polarization.

For future nodes of ferroelectric random access memory, but also for other densely packed applications the availability of a 3D-capable ferroelectric is of similarly high interest. FIG. 9 shows a TEM micrograph of a 3D-integrated, ferroelectric HZO thin film laminated with Al_2O_3. It clearly shows that a reasonable step coverage can be achieved and that the laminated structure is preserved down to the very bottom of the 1.6 μm deep trenches.

The P-V characteristics plotted for different trench counts in FIG. 10 provide electrical evidence that the effective area of the 3D capacitors is significantly increased compared to the projected 2D area and that therefore a stable ferroelectric phase is present along the sidewall of the trenches.

Although similar results with respect to the 3D scalability were obtain using Al:HfO_2,[4] $Hf_xZr_{1-x}O_2$ based materials provide a larger composition range showing ferroelectric behavior. In $Hf_xZr_{1-x}O_2$ system ferroelectricity was proven for x-ratios between 30 and 70 mol-% Zr,[9] while Al:HfO_2 only showed ferroelectricity between ~4-8 mol-% Al.[11] This increases the manufacturability for this material class. Additionally $Hf_xZr_{1-x}O_2$ films yield a higher remanent polarization than Al:HfO_2.

The broad process window for 3D-applications provided by the $Hf_xZr_{1-x}O_2$ system is elucidated by FIG. 11. Changing the cycle ratio for depositing the HZO layer from 1:1 to 2:3 reduces the Hf:Zr cation ratio determined by XPS from 60 cat-% Hf to 52 cat-%, while the remanent polarization on planar structures only changed by 10%. The remanent polarization decreases with increasing trench count i.e. with increasing 3D fraction of the capacitor. This is attributed to limited step coverage

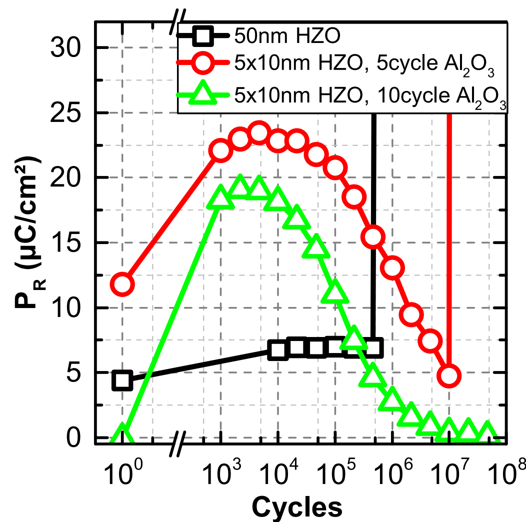

FIG. 8. Endurance of laminated and unlaminated 50nm HZO films. The laminated sample with 10 cycles of Al_2O_3 do not show dielectric break down until 10^8 cycles.

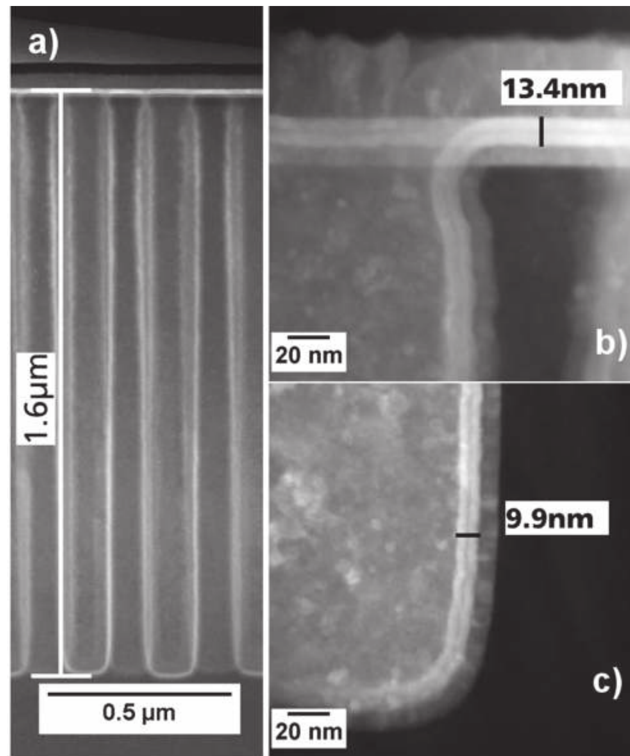

FIG. 9. HAADF STEM micrographs of Al_2O_3 laminated HZO thin films integrated into deep trench capacitors with an aspect ratio of ~11:1. a) Overview image b) high magnification image at trench top c) high magnification image at trench bottom. The step coverage of the employed HZO deposition process is ~75%.

of the used processes, which were not optimized for high aspect ratio structures as illustrated by FIG. 9. Since the film thickness is reduced at the trench bottom, the remanent polarization is reduced at the trench bottom causing a reduced mean polarization for 3D capacitors. However the remanent polarization, which is achieved using $Hf_xZr_{1-x}O_2$ films is still higher than values reported for Al:HfO_2 using the same capacitor structures.

It should be noted that laminating of the HZO layers is additionally required to withstand the increased thermal budget and corrosive chemistry which is applied during pCVD top TiN electrode deposition. 3D MFM capacitors consisting of unlaminated HZO films exhibit shorts between the top and the bottom electrode preventing any electrical characterization. This behavior furthermore proves that laminating HZO thin films improves the thermal stability of these films.

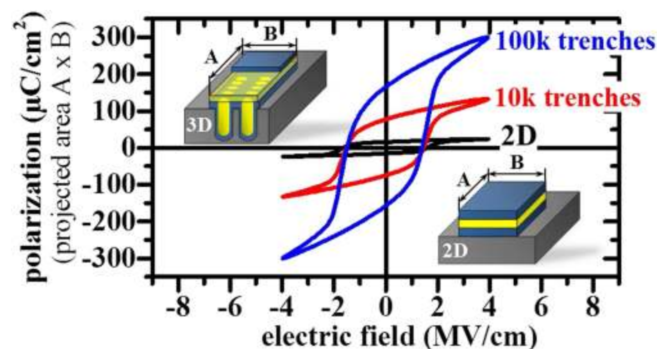

FIG. 10. P-V characteristics of 3D 2×5nm $H_{60}Z_{40}O$ (5cycles Al_2O_3) MFM capacitors with different trench-counts.

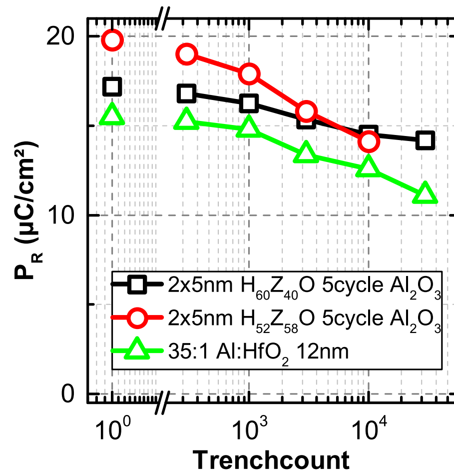

FIG. 11. Variation of the remanent polarization with increasing trench count of 3D capacitors. Al:HfO_2 data from 3. The actual capacitor area of the 3D MFM capacitors is calculated from measures taken from TEM crosssection depicted in FIG. 9.

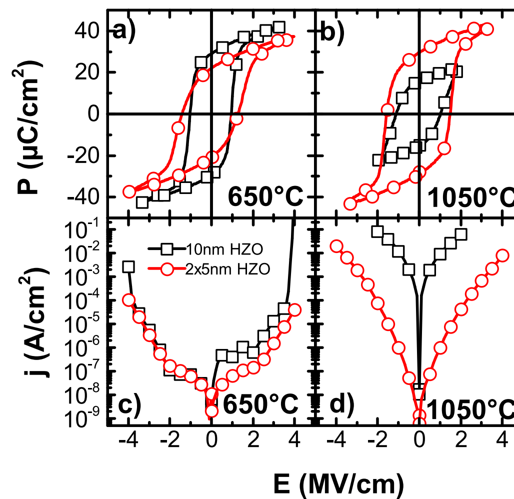

FIG. 12. P-E(a,b) and j-E(c,d) plots of a 10nm unlaminated and a 10nm laminated HZO sample subjected to rapid thermal anneals at 650°C (a,c) and 1050°C (b, d) 20s / N_2. The unlaminated sample degrades both in polarization and leakage by annealing at 1050°C.

Especially in the case of CMOS-processing, this high thermal stability is of equally high importance. In order to enable HZO as a gate material for ferroelectric field effect transistors or other ferroelectric devices implemented in the Front End of Line, the robustness of the material has to be maintained above 1000°C.

FIG. 12 illustrates the P-V as well as I-V behavior of an unlaminated and a laminated HZO film of equal composition. It is clearly observed that the Al_2O_3 interlayer reduces leakage as well as ferroelectric phase degradation. This improved behavior is once again attributed to the grain growth confinement and grain boundary interruption provided by the laminated structure.

IV. CONCLUSIONS

FE-HfO_2 provides the possibility to directly implement ferroelectric, pyroelectric or piezoelectric devices into standard CMOS technologies and therewith opens up a new pathway to advanced system on chip functionalization. The easy stoichiometry control, the excellent 3D-capability as well as the thickness independent ferroelectric characteristics of Al_2O_3 laminated $Hf_xZr_{1-x}O_2$ renders it the ideal

material to cope with a wide range of different applications. However, the impact of the additional interfaces introduced by the inserted Al_2O_3 layers on ferroelectric fatigue and retention needs to be further explored to fully judge the potential of this layered system.

ACKNOWLEDGMENTS

The work for this paper was supported by funding from the Free State of Saxony (Project: ARTEMIS, Project No:1001493891/2939). K. Biedermann and E. Reich are acknowledged for providing the TEM cross sections.

[1] M. H. Park, H. J. Kim, Y. J. Kim, T. Moon, K. D. Kim, and C. S. Hwang, Nano Energy **12**, 131 (2015).
[2] T. S. Boscke, J. Muller, D. Brauhaus, U. Schroder, and U. Bottger, in Electron Devices Meeting (IEDM), 2011 IEEE International (2011), p. 24.5.1-24.5.4.
[3] J. Müller, P. Polakowski, S. Mueller, and T. Mikolajick, ECS Journal of Solid State Science and Technology **4**, N30–N35 (2015).
[4] P. Polakowski, S. Riedel, W. Weinreich, M. Rudolf, J. Sundqvist, K. Seidel, and J. Muller, in Memory Workshop (IMW), 2014 IEEE 6th International (2014), p. 1–4.
[5] J. Muller, E. Yurchuk, T. Schlosser, J. Paul, R. Hoffmann, S. Muller, D. Martin, S. Slesazeck, P. Polakowski, J. Sundqvist, M. Czernohorsky, K. Seidel, P. Kucher, R. Boschke, M. Trentzsch, K. Gebauer, U. Schroder, and T. Mikolajick, in VLSI Technology (VLSIT), 2012 Symposium on (2012), p. 25–26.
[6] C. H. Cheng and A. Chin, *Electron Device Letters* (IEEE, 2014), **35**, p. 274.
[7] M. H. Park, H. J. Kim, Y. J. Kim, T. Moon, K. D. Kim, and C. S. Hwang, Adv. Energy Mater. **4** (2014) n/a.
[8] J. Muller, T. S. Boscke, S. Muller, E. Yurchuk, P. Polakowski, J. Paul, D. Martin, T. Schenk, K. Khullar, A. Kersch, W. Weinreich, S. Riedel, K. Seidel, A. Kumar, T. M. Arruda, S. V. Kalinin, T. Schlosser, R. Boschke, R. van Bentum, U. Schroder, and T. Mikolajick, in Electron Devices Meeting (IEDM), 2013 IEEE International (2013), p. 10.8.1-10.8.4.
[9] J. Müller, T. S. Böscke, U. Schröder, S. Mueller, D. Bräuhaus, U. Böttger, L. Frey, and T. Mikolajick, Nano Lett. **12**, 4318 (2012).
[10] M. H. Park, Y. H. Lee, H. J. Kim, Y. J. Kim, T. Moon, K. D. Kim, J. Müller, A. Kersch, U. Schroeder, T. Mikolajick, and C. S. Hwang, Adv. Mater **27**, 1811 (2015).
[11] S. Mueller, J. Mueller, A. Singh, S. Riedel, J. Sundqvist, U. Schroeder, and T. Mikolajick, Advanced Functional Materials **22**, 2412 (2012).
[12] H. J. Cho, Y. D. Kim, D. S. Park, E. Lee, C. H. Park, J. S. Jang, K. B. Lee, H. W. Kim, Y. J. Ki, I. K. Han, and Y. W. Song, Solid-State Electronics **51**, 1529 (2007).
[13] H. J. Kim, M. H. Park, Y. J. Kim, Y. H. Lee, W. Jeon, T. Gwon, T. Moon, K. D. Kim, and C. S. Hwang, Applied Physics Letters **105** (2014).
[14] S.-G. Kim, S. Priya, and I. Kanno, MRS Bull. **37**, 1039 (2012).
[15] S. Starschich, D. Griesche, T. Schneller, R. Waser, and U. Böttger, Applied Physics Letters **104** (2014).
[16] O. Bierwagen, L. Geelhaar, X. Gay, M. Piešiņš, H. Riechert, B. Jobst, and A. Rucki, Applied Physics Letters **90** (2007).
[17] J. Robertson, Rep. Prog. Phys. **69**, 327 (2006).